IEEE Access
Multidisciplinary : Rapid Review : Open Access Journal

Received June 23, 2020, accepted July 2, 2020, date of publication July 13, 2020, date of current version July 23, 2020.

Digital Object Identifier 10.1109/ACCESS.2020.3008695

Impervious Surface Extraction by Linear Spectral Mixture Analysis with Post-Processing Model

YI ZHAO[1,2,5], JIANHUI XU[2,3], KAIWEN ZHONG[2,4], YUNPENG WANG[1,5], HONGDA HU[2,3], AND PINGHAO WU[1,2,5]

[1]Guangzhou Institute of Geochemistry, Chinese Academy of Sciences, Guangzhou 510640, China
[2]Key Laboratory of Guangdong for Utilization of Remote Sensing and Geographical Information System, Guangdong Open Laboratory of Geospatial Information Technology and Application, Guangzhou Institute of Geography, Guangzhou 510640, China
[3]Southern Marine Science and Engineering Guangdong Laboratory (Guangzhou), Guangzhou 510640, China
[4]Guangdong Science and Technology Collaborative Innovation Center for Natural Resources, Guangzhou 510070, China
[5]College of Resource and Environment, University of Chinese Academy of Sciences, Beijing 100049, China

Corresponding author: Kaiwen Zhong (zkw@gdas.ac.cn)

This work was supported in part by the Key Special Project for Introduced Talents Team of Southern Marine Science and Engineering Guangdong Laboratory (Guangzhou) under Grant GML2019ZD0301, in part by the National Natural Science Foundation of China under Grant 41901371, in part by the Science and Technology Planning Project of Guangdong Province under Grant 2018B020207012, Grant 2018B020207002, Grant 2019B020208004, and Grant 2019B020208013, in part by the Guangdong Innovative and Entrepreneurial Research Team Program under Grant 2016ZT06D336, in part by the Guangdong Academy of Sciences (GDAS) Project of Science and Technology Development under Grant 2018GDASCX-0403, Grant 2019GDASYL-0301001, and Grant 2019GDASYL-0501001, and in part by the Guangdong Provincial Agricultural Science and Technology Innovation and Extension Project under Grant 2019KJ147.

ABSTRACT Accurate estimations of impervious surface areas are essential for urban planning development. Linear spectral mixture analysis (LSMA) is commonly adopted to extract the impervious surface (IS) fraction in a mixed pixel at the subpixel scale. However, owing to errors in the spectra of pure pixels selected from remote sensing images, incorrect fractions of different land cover types often emerge after unmixing. In this study, two Landsat 8 Operational Land Imager (OLI) images—acquired on 20 September 2019 (Path/Row: 121/44) and 14 November 2019 (Path/Row: 122/44)—of Guangzhou and Shenzhen were unmixed by LSMA using spectral indices in endmember selection. A post-processing model using the Dry Bare-soil Index (DBSI) and Normalized Difference Vegetation Index (NDVI) as thresholds was established to improve the IS fraction of the LSMA result. Comparative analysis reveals that LSMA with the post-processing model achieves better performance for IS fraction extraction ($R^2 = 0.910$ and 0.926 and root mean square error [RMSE] $= 10.08\%$ and 10.83% for Guangzhou and Shenzhen, respectively), and the distribution of IS is basically consistent with the IS of the actual areas. The post-processing model solves the problem of overestimation of pervious surface and underestimation of impervious surface.

INDEX TERMS Impervious surface, post-processing model, DBSI, linear spectral mixture analysis.

I. INTRODUCTION

Urban development is accompanied by the generation of impervious surfaces (IS) [1]–[3], which replace permeable surfaces such as vegetation or soil and represent symbolic and typical products of urbanization [4], [5]. An IS is defined as any surface of artificial material (or a combination of materials) that cannot be infiltrated (e.g., buildings and roads constructed using cement and asphalt) [6]; major increases in such surfaces directly impact the environment [7]. For example, the expansion of urban surface creates an urban heat island [8], [9] and changes surface runoff, important contributors to urban waterlogging [10] and rainstorms [3], [10], [11]. Therefore, it is of great significance to study IS, especially in urban areas.

In recent years, many studies on urban IS [12]–[15] and its environmental effect [16] have been conducted. In order to calculate the area of IS, the subpixel linear spectral mixture analysis (LSMA) based on the V-I-S model [17]–[20] is commonly employed. Owing to spatial resolution, some pixels from remote sensing images (e.g., Landsat imagery with 30 m spatial resolution) contain different land cover types, termed mixed pixels. In calculating the IS, the LSMA considers the fraction of each land cover type in a mixed pixel. It is assumed that the spectral signal of a mixed pixel is a linear combination of the endmember spectral signals

The associate editor coordinating the review of this manuscript and approving it for publication was Wenming Cao.

of each component [21], and the mixed pixel comprises vegetation, soil, and the high- and low-albedo IS. In LSMA unmixing results, IS is considered as a blend of high- and low-albedo [22]. During endmember selection, as mixed pixels and the interrelationships of different spectra, the IS fraction from LSMA can be overrated in some areas where the IS coverage is lower than 20% [23], and underestimated where it is close to 100% [24].

During LSMA, the pure endmember selection is a significant step [19], [25] since the spectral information of different endmembers represent the corresponding land cover types in a mixed pixel for unmixing [26]. This implies that, the closer the spectral curve of a mixed pixel is to that of a pure endmember, the higher the coverage of such land cover type in the mixed pixel [27]. The two sources of pure endmembers are the spectral library and actual remote sensing images. However, for multispectral imagery, the endmember selection from a mixed pixel can be difficult because of the low spatial and spectral resolution [28]. Several studies on improving the endmembers selection accuracy [29]–[31] such as the N-Finder algorithm and Endmember average RMSE (EAR) [32] are available. Thus far, the problems arising from endmember selection are summarized as follows:

1. Pure endmember selection is difficult where remote sensing images of medium resolution containing mixed land cover types and/or are influenced by environmental factors such as cloud cover.

2.Unmixing errors arise from spectral information similarity for different land cover types in certain bands.

3.Unmixing errors are also caused by reflectance from standard spectral libraries because the spectral information of each land cover type can be influenced by multiple factors in different study areas.

4.Available high-spatial-resolution remote sensing images include fewer bands, thereby providing little information for LSMA unmixing.

Spectral indices, including the high-albedo and low-albedo from images after the tasseled cap transformation, Normalized Difference Vegetation Index (NDVI) [33], Normalized Difference Built-up Index (NDBI) [34], and Ratio Normalized Difference Soil Index (RNDSI) [35], have been applied for endmember selection and extraction in 2019 by Li [36]. The results showed that spectral indices enable more rapid and reliable target endmember selection, producing extracted IS fractions of improved accuracy. However, this approach fails to eliminate mixing errors caused by the interaction between the spectra of different land cover types and by environmental factors, with misclassification in unmixing results persisting. As the spectral curves of high-albedo IS and soil are similar, some IS are misclassified as soil by conventional LMSA and by the LMSA of Li *et al.* [36], while the IS component also contains misclassified vegetation and soil components.

In this study, the Dry Bare-Soil Index (DBSI) [37] replaced the RNDSI for endmember selection because, in the study areas, soil pixel DBSI values are higher, and the differences between soil and IS pixels are greater than those for RNDSI with identical pixels.

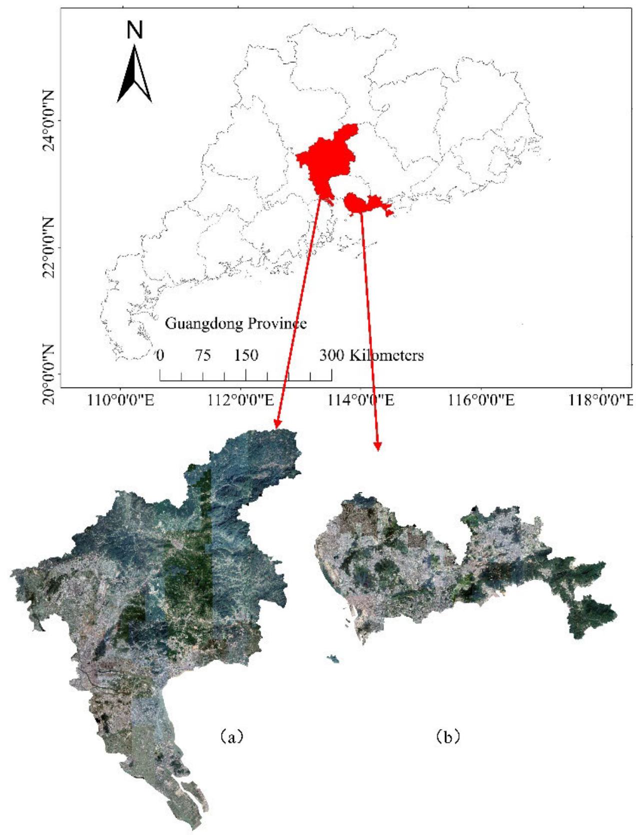

FIGURE 1. RGB images of the study areas: (a) Guangzhou, and (b) Shenzhen from Google Earth.

In addition, a post-processing model for optimizing the unmixing result of LSMA was developed. In this model, NDVI and DBSI thresholds are applied to separate the IS fraction from the soil and vegetation fractions. Our post-processing model solved the problem of overestimation in pervious surface and the underestimation in the impervious surface for IS fraction. The LSMA with post-processing model can extract the IS fraction with high precision, and thus provides reliable data support for studies into urban change monitoring and quantitative environmental analysis. As such, our results are of great significance for urban development and planning.

II. STUDY AREA AND DATA

A. STUDY AREA

Guangdong province, southern China, has a long cultural history and prosperous economy. Guangzhou (112°57 'E–114°30' E; 22°26 'N–23°56' N), the capital of Guangdong province (Figure 1), is a megacity at the center of the Guangdong-Hong Kong-Macao Greater Bay Area. It is a major hub of the One Belt and One Road in the Pearl River Delta economic zone. At the end of 2019, the population of Guangzhou was 15.3059 million, with an urbanization rate (UR) of 86.46%. At present, it comprises

11 districts, with the study area covering 6, including Baiyun (UR 81.04%), Huangpu (UR 91.66%), Tianhe (UR 100%), Yuexiu (UR 100%), Liwan (UR 100%), and Haizhu (UR 100%) [38]. The study area includes the Central Business District and extensive agricultural land as well as forest and mountain areas with high vegetation cover (i.e., land use types are diverse and the IS displays obvious characteristics).

Shenzhen is a smaller city in Guangdong province, with plans for its development into a megacity. At the end of 2019, the city comprised 9 districts and had a built-up area of 927.96 m^2 out of a total 1997.47 m^2. The population was 13.026 million and the UR was 100%, the first city in China to reach this milestone [39].

B. DATA

Extracting IS information from remote sensing images is vital for quantitative urban analysis. In this study, Landsat 8 Operational Land Imager (OLI) images acquired on 20 September 2019 (Path/Row: 121/44) and 14 November 2019 (Path/Row: 122/44) were employed for IS extraction. Google Earth images with 2.19-m spatial resolution from 31 October 2019 were used to vectorize samples for accuracy assessment of IS extraction results.

The Landsat 8 satellite, launched in February 2013, contains an OLI and a Thermal Infrared Sensor (TIR). The Landsat 8 OLI image comprises nine reflective wavelength bands, including seven 30-m visible, NIR, and SWIR bands, and a 15-m panchromatic band. Bands 1–7, used in this study, correspond to the coastal, blue, green, red, near infrared, short-wave infrared I, and short-wave infrared II bands, with spatial resolution of 30 m, as presented in Table 1. The surface reflectance products of the Landsat 8 OLI images without cloud cover were ordered and downloaded from the United States Geological Survey (USGS) Earth Resources Observation and Science's (EROS) Science Processing Architecture (ESPA) on Demand Interface (https://espa.cr.usgs.gov) [3]. The products were geometrically rectified to a Universal Transverse Mercator (UTM) projection system (zone 49 N). Landsat 8 OLI surface reflectance values were generated using the Land Surface Reflectance Code (LaSRC) algorithm (Version 1.4.1), utilizing the coastal aerosol band to perform aerosol inversion tests, auxiliary climate data from the Moderate Resolution Imaging Spectroradiometer (MODIS), and a radiative transfer model [40].

TABLE 1. Bands of Landsat images.

Band	Resolution(m)	Wavelength(μm)
B1	30	0.433–0.453
B2 (Blue)	30	0.450–0.515
B3 (Green)	30	0.525–0.600
B4 (Red)	30	0.630–0.680
B5 (NIR)	30	0.845–0.885
B6 (SWIR 1)	30	1.560–1.660
B7 (SWIR 2)	30	2.100–2.300

III. METHODS

The workflow for the method proposed in this study is as follows (Figure 2): (1) endmember selection using spectral indexes; (2) unmixing by LSMA; and (3) IS fraction extraction accuracy improvement using the post-processing model.

Before calculating the spectral indices, pixels with surface reflectance values of less than 0 and greater than 1 in the image were corrected to 0 and 1 by pre-processing of the Landsat 8 OLI surface reflectance product after geometric correction. Based on the V-I-S model, water bodies, including rivers, lakes, reservoirs, and others were removed from the remote sensing images to prevent noise and reduce unmixing errors caused by low albedo IS [36], [41]. The Modified Normalized Difference Water Index (MNDWI) [42] was used to eliminate water bodies in the study area, while the Otsu algorithm [43] was used to determine threshold values. The MNDWI was calculated from the following expression:

$$MNDWI = \frac{\rho_{Green} - \rho_{SWIR1}}{\rho_{Green} + \rho_{SWIR1}} \tag{1}$$

where ρ_{Green} and ρ_{SWIR1} are the reflectance of bands 3 (the green band) and 6 (the near-infrared band), respectively, of the Landsat imagery.

A. ENDMEMBER SELECTION IMPROVEMENT

For IS extraction by LSMA, endmember selection is a key step. In conventional LSMA, Minimum Noise Fraction (MNF) rotation is usually employed to remove noise in the remote sensing images; relatively pure pixels are then selected by introducing the Pixel Purity Index (PPI) [44], [45], with the PPI value proportional to the pixel purity [46]. Alternatively, Li *et al.* [36] proposed endmember selection from the spectral indices of the images, and used the NDVI, NDBI, RNDSI, high- and low-albedo (from images after tasseled cap transformation) to select the spectral curve of endmembers.

In this study, five spectral indices of the Landsat images, including the NDVI, NDBI, DBSI, high albedo (H), and low albedo (L), were overlain as layers. According to the characteristics of these indices, the target endmembers were then selected. Endmembers selection was conducted through the N-dimensional visualization window of the ENVI (v. 5.3) software. The generalized expressions for calculating these spectral indices were as follows:

$$NDVI = \frac{\rho_{NIR} - \rho_{R}}{\rho_{NIR} + \rho_{R}} \tag{2}$$

$$NDBI = \frac{\rho_{SWIR1} - \rho_{NIR}}{\rho_{SWIR1} + \rho_{NIR}} \tag{3}$$

$$DBSI = \frac{\rho_{SWIR1} - \rho_{GREEN}}{\rho_{SWIR1} + \rho_{GREEN}} - NDVI \tag{4}$$

where ρ_{Green}, ρR, ρ_{NIR}, and ρ_{SWIR1} are the reflectances of bands 3 (the green band), 4 (the red band) 5, and 6 (the near-infrared band), respectively, of the Landsat imagery. Then, tasseled cap transformation [47] of the Landsat 8 OLI was

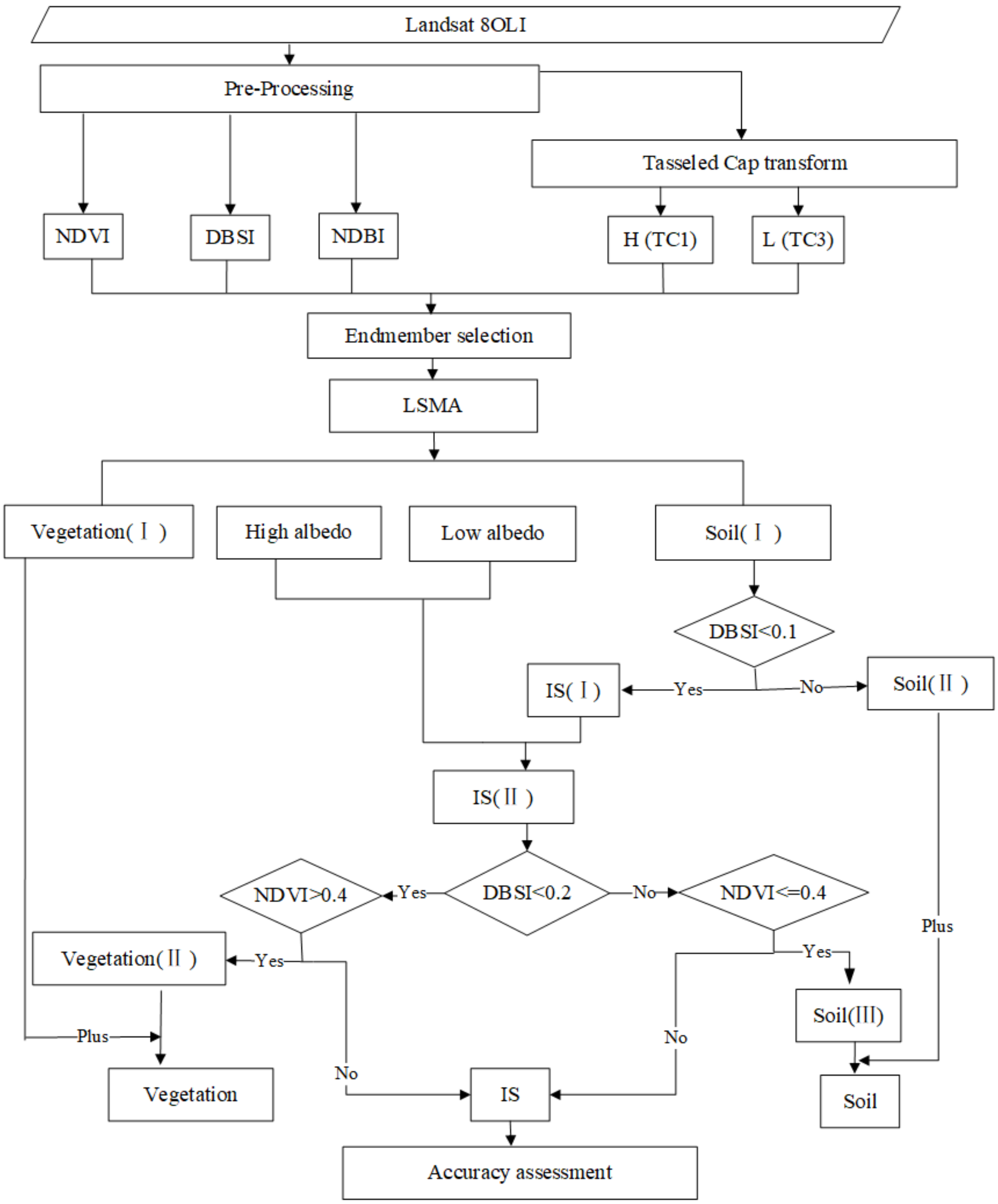

FIGURE 2. **Flowchart of improved linear spectral mixture analysis.**

applied for calculating the high albedo and the low albedo given as:

$$H = \frac{TC1 - TC1_{min}}{TC1_{max} - TC1_{min}} \tag{5}$$

$$L = \frac{TC3 - TC3_{min}}{TC3_{max} - TC3_{min}} \tag{6}$$

where H and L are the high albedo and low albedo from the biophysical composition index (BCI), respectively [48], [49]. The parameter TC_1 is the first component and TC_3 is the third component of the Landsat image after tasseled cap transformation; TC_{1min} is the minimum value of TC_1, and TC_{1max} is the maximum value of TC_1; TC_{3min} is the minimum value of TC_3, and TC_{3max} is the maximum value of TC_3.

B. CONVENTIONAL LINEAR SPECTRAL MIXTURE ANALYSIS

Since mixed pixels are ubiquitous in remote sensing images, in LSMA, the reflectance of a mixed pixel is considered a linear combination of the reflectance of its endmembers, expressed as follows:

$$\begin{cases} R_i = \sum_{k-1}^{n} f_k R_{ik} + ER_{ik} \\ \sum_{k=1}^{n} f_k = 1 \\ f_k \geq 0 \end{cases} \tag{7}$$

where $i = 1, 2 \ldots, \mathrm{M}$, with M denoting the band number; $k = 1, 2, \ldots; n$ is an index of endmembers, with n representing the number of endmembers; R_i is the spectral reflectance of band i within a mixed pixel; f is the fraction of the endmember k; and ER_i is the residual error of band i.

The RMS was used to assess the accuracy of the LSMA; the value is inversely proportional to precision and is expressed as:

$$RMS = \left(\frac{\sum_{i=1}^{M} ER_i^2}{M}\right)^{1/2} \tag{8}$$

where ER_i is the residual error and M is the number of the spectral band.

C. POST-PROCESSING MODEL

For the results of conventional LSMA, owing to endmember spectral errors, nonnegligible errors emerge for the fractions of different land cover types in mixed pixels. In LSMA results, confusion between soil and the IS fraction is frequent, with large amounts of vegetation and soil fractions common in the IS fraction. To reduce such errors, a post-processing model was developed in this study. This model is based on the pixel scale.

(1) First, the IS fraction (IS I in Figure 2) was extracted from the soil fraction of the unmixing result through the DBSI threshold value. The higher the DBSI value, the higher the proportion of soil in the pixel. In previous studies, a DBSI value of 0.26 [37] has served as the threshold dividing bare soil from other land cover types. To enhance reliability of the soil fraction in unmixing results as much as possible, a DBSI image value histogram was created. According to the trough and peak of the histogram and multiple tests, a DBSI threshold value of 0.1 was determined for separating the IS from the soil component (pixels with DBSI value less than 0.1 in the soil fraction were divided into IS). The expression for calculating that IS I fraction was as follows:

$$IS_I = Soil_I, \quad if\ DBSI < 0.1 \tag{9}$$

(2) Next, we added the IS fraction (IS I) separated from the soil fraction to the IS fraction of the unmixing result. The high and low albedo fractions of the unmixing results were added to produce the IS fraction of the unmixing result. Then, the IS fraction of the unmixing result was added to IS I from step 1 to obtain a new IS fraction (IS II in Figure 2) containing misclassified vegetation and soil fractions. The expression for calculating the IS II fraction was as follows:

$$IS_{II} = IS_I + High\ albedo + Low\ albedo, \tag{10}$$

(3) Finally, we removed the vegetation and soil fractions from the IS fraction (IS II) obtained in step 2 using the NDVI and DBSI threshold value. In previous studies, negative NDVI values are likely water, and the NDVI value is close to +1, it will be vegetation, while the value is close to 0, it will be soil or desertified land. In order to extract relatively pure soil and vegetation pixels, according to the histogram trough and peak values for the DBSI and NDVI images, including multiple testing, an NDVI value of 0.4 and DBSI value of 0.2 were utilized as thresholds for separating vegetation and soil, respectively, from the IS fraction. The expression for calculating the final IS fraction was as follows:

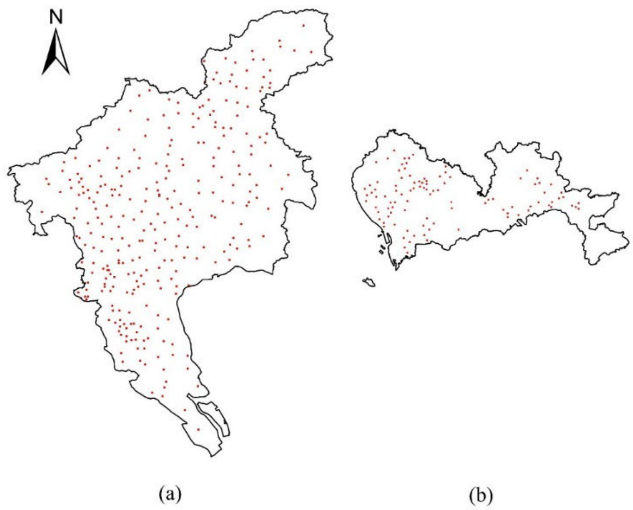

FIGURE 3. Distribution of samples distribution in: (a) Guangzhou and (b) Shenzhen.

$$\begin{cases} IS = IS_{II} - Vegetation_{II} - Soil_{III}, \\ Vegetation_{II} = IS_{II}, \quad if\ DBSI < 0.2\ and\ NDVI > 0.4, \\ Soil_{III} = IS_{II}, \quad\quad if\ DBSI > 0.2\ and\ NDVI < 0.4. \end{cases} \tag{11}$$

Details of the modified processing method are displayed in Figure 2.

D. ACCURACY ASSESSMENT

In this study, the spectral indices for endmember selection proposed by Li *et al.* [36] were applied for LSMA; thus, in the comparative analysis, the LSMA proposed by Li *et al.* [36] and conventional LSMA were implemented to illustrate the performance of LSMA with our post-processing model. A total of 350 samples (250 samples from Guangzhou and 100 samples from Shenzhen; Figure 3) with a spatial resolution of 480 × 480 m were selected randomly, and Google Earth images were used to digitize the IS coverage. The IS fraction of each sample was calculated by dividing the IS area by the total sample area (230,400 m^2). The Root Mean Square Error (RMSE), Mean Absolute Error (MAE), and Systematic Error (SE) were then computed to test for accuracy using the following formula:

$$SE = \frac{\sum_{i=1}^{N}\left(X_i - \hat{X}_i\right)}{N}, \tag{12}$$

$$MAE = \frac{\sum_{i=1}^{N}\left(\left|X_i - \hat{X}_i\right|\right)}{N}, \tag{13}$$

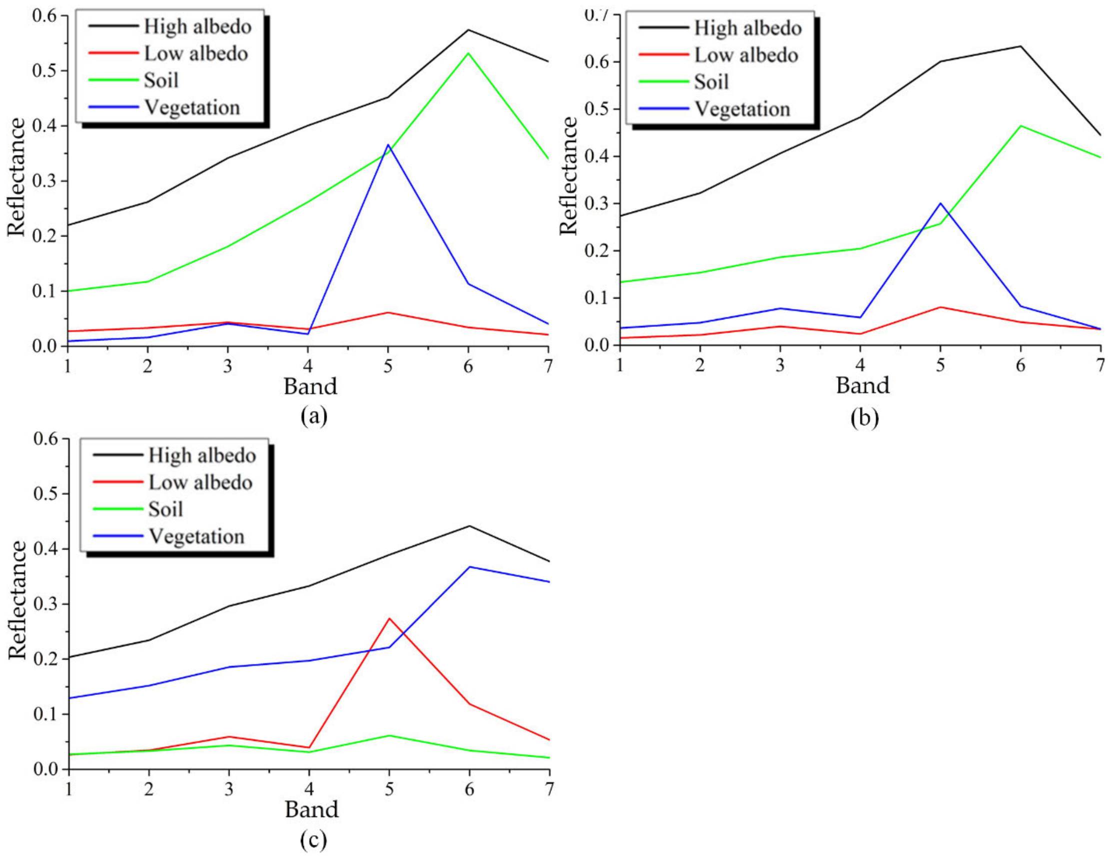

FIGURE 4. Spectral curve of endmembers selected by: (a) the spectral indices (NDVI, NDBI, DBSI, H and L) proposed in this study, (b) the spectral indices (NDVI, NDBI, RNDSI, H and L) proposed by Li, and (c) MNF and PPI in conventional LSMA.

$$RMSE = \sqrt{\frac{\sum_{i=1}^{N}\left(X_i - \hat{X}_i\right)}{N}}. \tag{14}$$

where X_i is the IS fraction of the LSMA of the Landsat 8 OLI data and $\hat{X}_i$ is the IS fraction of sample i. The RMSE and MAE provided relative errors for fractional IS estimates, whereas the SE served as a bias indicator, measuring the overall error between the IS fraction of the Landsat 8 OLI data and the IS fraction of the Google Earth images. Additionally, results of spectra for some test images were also examined.

IV. RESULTS

A. ENDMEMBER SELECTION

The spectral curves of endmembers selected in different ways and based on the two Landsat 8 images are shown in Figure 4. Since the locations and acquisition times of the images were close, the same endmember spectra (Figure 4a) were applied as basis for the LSMA with the post-processing model. The IS fractions of the LSMA techniques (Figure 5) illustrate the feasibility of the approach. The selected indices (see section 3.2) exhibit different sensitivities for various land cover types, and their combination contributed meaningfully when selecting endmembers. It was found that NDBI values are lower than DBSI values in bare soil pixels, but are close to DBSI values for IS. The NDVI values are higher than the other indices in regions with higher vegetation coverage, while DBSI values are higher than the other indices in regions with higher soil coverage. The H and L (denoting high and low albedo) IS represent the IS in most studies of urban IS. Through the plot window in ENVI, endmembers for vegetation, soil, H, and L were selected and spectral curves of these endmembers for LSMA were produced. Figure 4(b) shows the spectral curves of endmembers selected by the Li *et al.* [36] LSMA; the spectral reflectances of vegetation and soil in bands 5 and 6 were underestimated, while the spectral reflectance of the high-albedo IS were overestimated. Figure 4(c) shows the spectral curves of endmembers selected by the MNF rotation and PPI. According to the PPI results, the number of pixels with values greater than 10 was small; therefore, endmember selection was not effortless. By comparing the spectral information of endmembers selected using the LSMA with the post-processing model, the Li *et al.* [36] LSMA, and the conventional LSMA, the spectral curves of each land cover type were closer to the actual spectral curve in Figure 4(a), although the spectral curves for the H and vegetation were lower than the actual curves in Figure 4(b).

B. COMPARATIVE ANALYSIS

Using the spectral curves of the endmembers, IS fraction maps (Figure 5) were created by the Li's, conventional

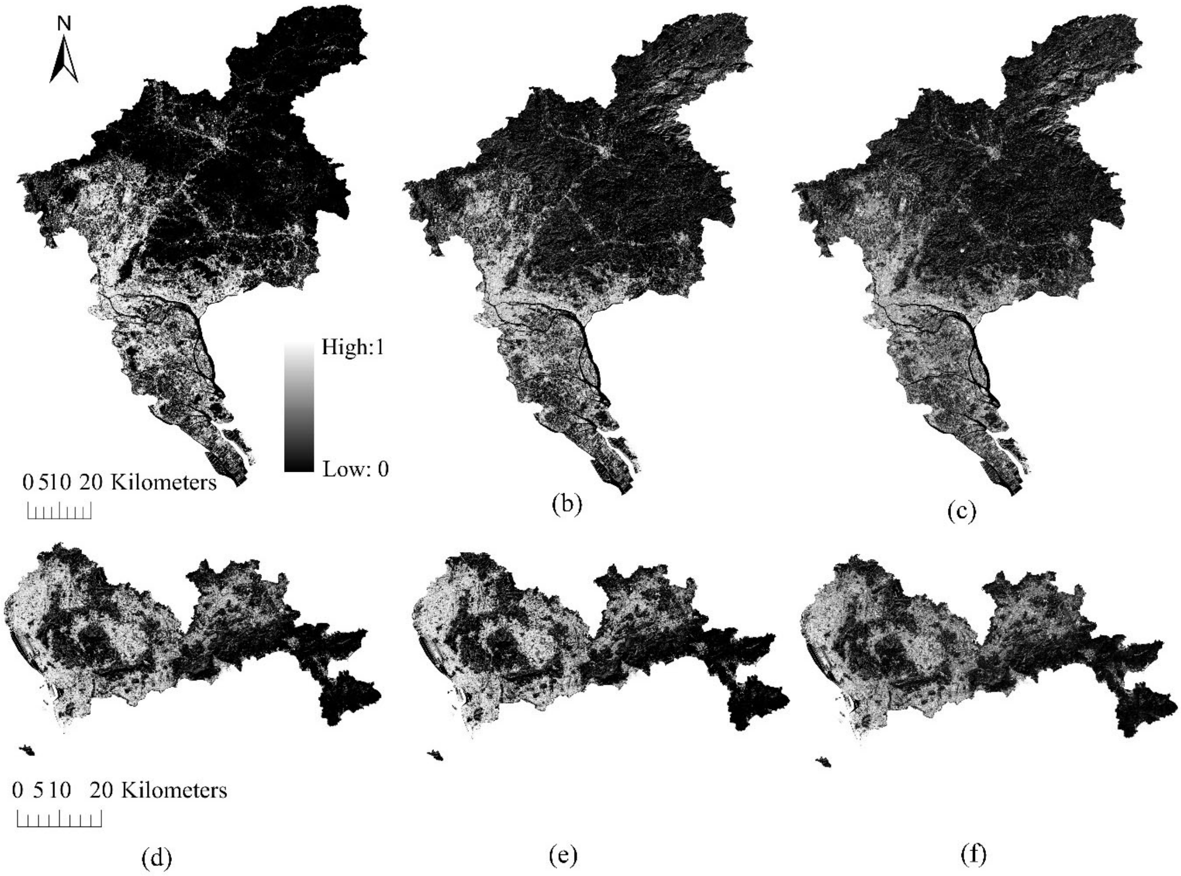

FIGURE 5. Impervious surface fraction extracted by: (a, d) the LSMA with Post-processing model, (b, e) the Li's LSMA, (c, f) the conventional LSMA.

TABLE 2. Accuracy assessment of impervious surface fraction extracted by the proposed method and the conventional LSMA.

Study area	Method	SE	MAE	RMSE	R^2
Guangzhou	LSMA with Post-processing model	0.002	0.065	0.101	0.910
	Li's LSMA	-0.019	0.124	0.169	0.764
	Conventional LSMA	-0.029	0.152	0.192	0.755
Shenzhen	LSMA with Post-processing model	-0.019	0.073	0.108	0.926
	Li's LSMA	-0.079	0.138	0.175	0.876
	Conventional LSMA	-0.115	0.191	0.234	0.819

LSMA, and LSMA with the post-processing model; the latter showed the best extraction performance. In pervious areas (forest, farmland, etc.), the conventional and Li's LSMAs overestimated IS, with the IS fractions higher than those by the LSMA with Post-processing model. Conversely, in developed areas (e.g., the Tianhe district of Guangzhou, Nanshan district of Shenzhen), the conventional and Li's LSMAs underestimated IS fractions relative to LSMA with the post-processing model proposed in this study.

The accuracy of the LSMA with the post-processing model was obviously higher than that of the conventional and Li's LSMAs. From Figure 6 and Table 2, in Guangzhou, for the LSMA with the post-processing model, R^2 was 20.5% higher than that of the conventional LSMA, and 19.1% higher than that of Li's LSMA. In particular, the SE value from LSMA with the post-processing model was 0.002, meaning that the distribution of IS fractions extracted by this method almost matched the actual IS. Furthermore, the MAE from LSMA with the post-processing model was 57.2% lower than that of the conventional LSMA, and 47.6% lower than that of the Li's LSMA, while the RMSE was 47.4% and 40.2% lower than those of the conventional and Li's LSMAs.

For Shenzhen, the R^2 for the LSMA with the post-processing model was 13.1% and 5.1% higher than those for the conventional and Li's LSMAs, respectively. The SE (-0.019) also confirmed improved performance, with

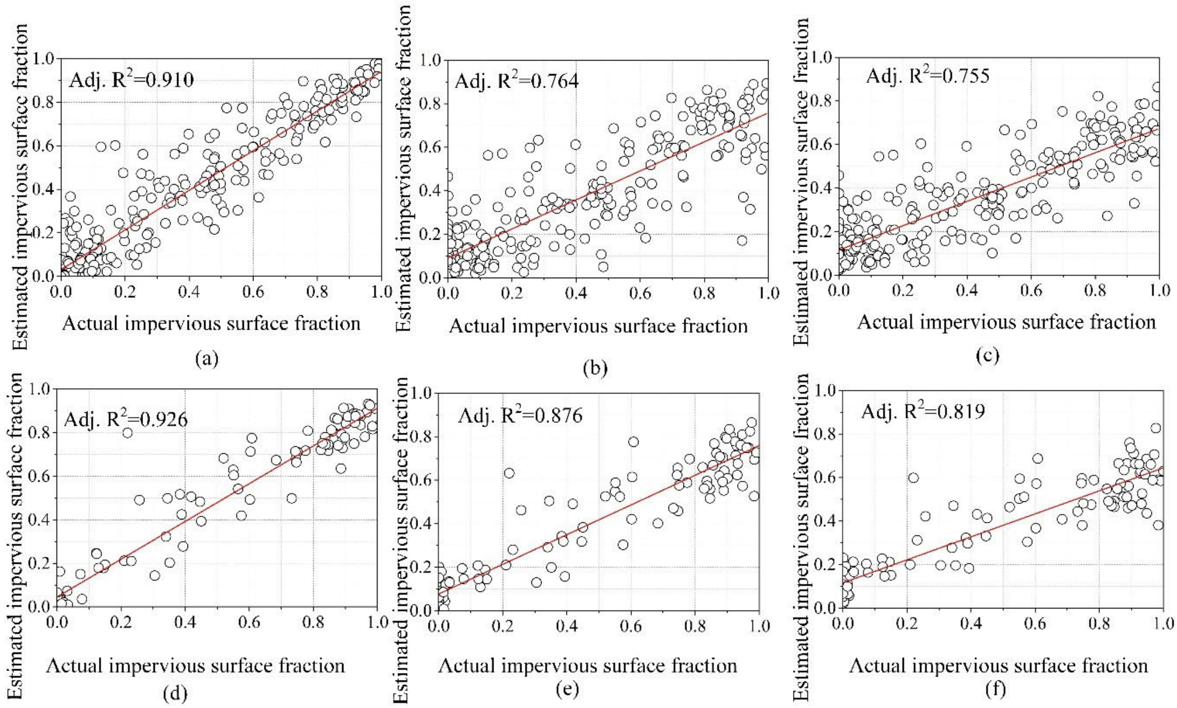

FIGURE 6. Linear fitting Scatterplot of the actual impervious surface fraction and the estimated impervious surface fraction extracted by: (a) the LSMA with Post-processing model, (b) Li's LSMA, (c) the conventional LSMA in Guangzhou; (d) the LSMA with Post-processing model, (e) the Li's LSMA, (f) the conventional LSMA in Shenzhen.

MAE values that were 61.8% and 47.1% lower than those of the conventional and Li's LSMA, respectively. Finally, the RMSE from the LSMA with the post-processing model was 53.8% and 38.3% lower than those of the conventional and Li's LSMAs, respectively.

V. DISCUSSION

In this study, NDVI, NDBI, DBSI, H, and L were applied to improve endmember selection. DBSI was used instead of RNDSI, which was proposed by Li *et al.* [36], because the DBSI can better distinguish soil, vegetation, and IS within different land cover types, and more conducive to the separation of the IS fraction from LSMA results using the post-processing model proposed in this study. To further illustrate the difference, the distribution maps of RNDSI and DBSI for Guangzhou and Shenzhen are shown in Figure 7. Based on statistical and visual analyses, soil pixels display the highest DBSI values, followed by IS pixels; vegetation pixels show the lowest values. In the DBSI distribution images, areas covered by vegetation are clearly demarcated from those of soil and IS. The differences between these three land cover types facilitates the application of LSMA with the post-processing model proposed in section 3.1 and 3.3. Conversely, in the RNDSI distribution images, vegetation pixels show the highest values, followed by IS surface pixels, and then the soil pixels.

Owing to similar spectral characteristics for soil and high albedo IS, these two fractions are often misclassified by LSMA. However, in the DBSI distribution image, IS is easily

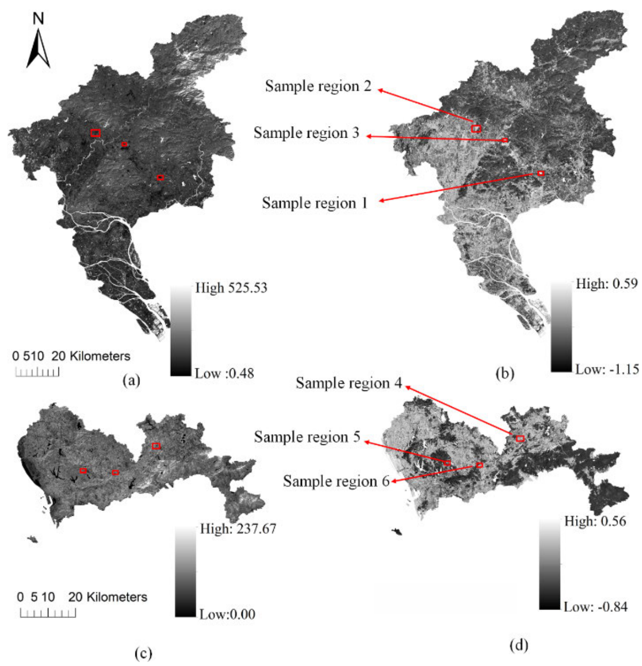

FIGURE 7. Distribution of: (a, c) Ratio Normalized Difference Soil Index (RNDSI), (b, d) Dry Bare-Soil Index (DBSI). And locations of the sample regions for details.

separated from the soil fraction based on spectral differences. According to sampling statistics, the difference between IS and soil in the DBSI distribution image surpasses that in the RNDSI image. Therefore, DBSI emerges as a more suitable index for differentiating soil and IS. To compare the

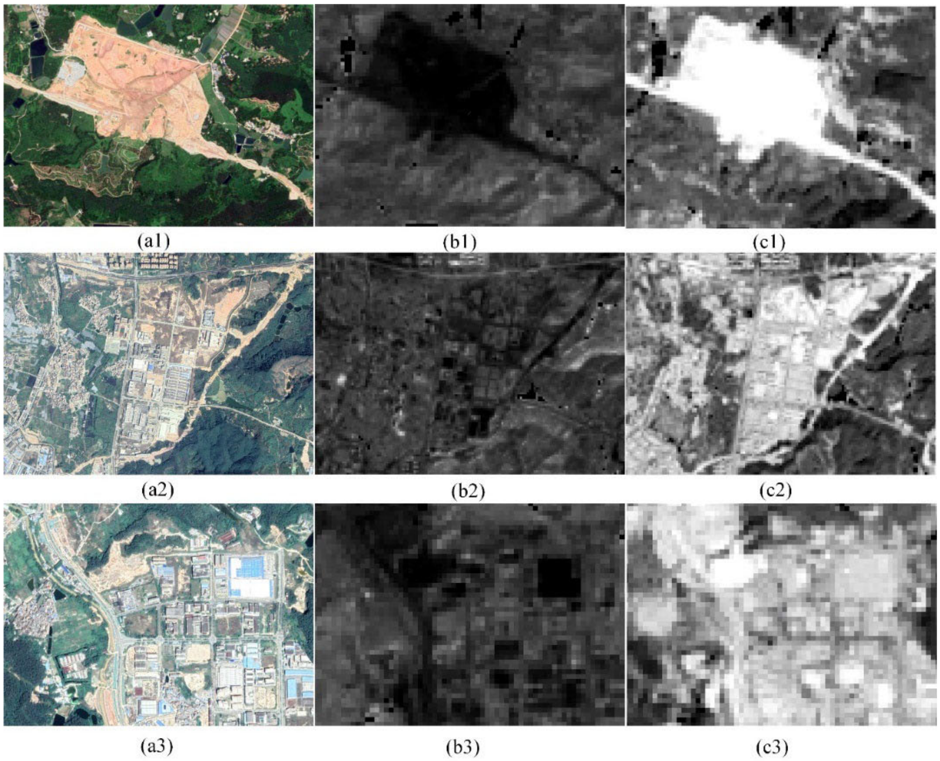

FIGURE 8. Mapping of: (a1∼ a3): Google Earth image, (b1∼b3): the value of RNDSI, (c1∼ c3) the value of DBSI in (a1∼c1): sample region 1, (a2∼c2): sample region 2 in Guangzhou.

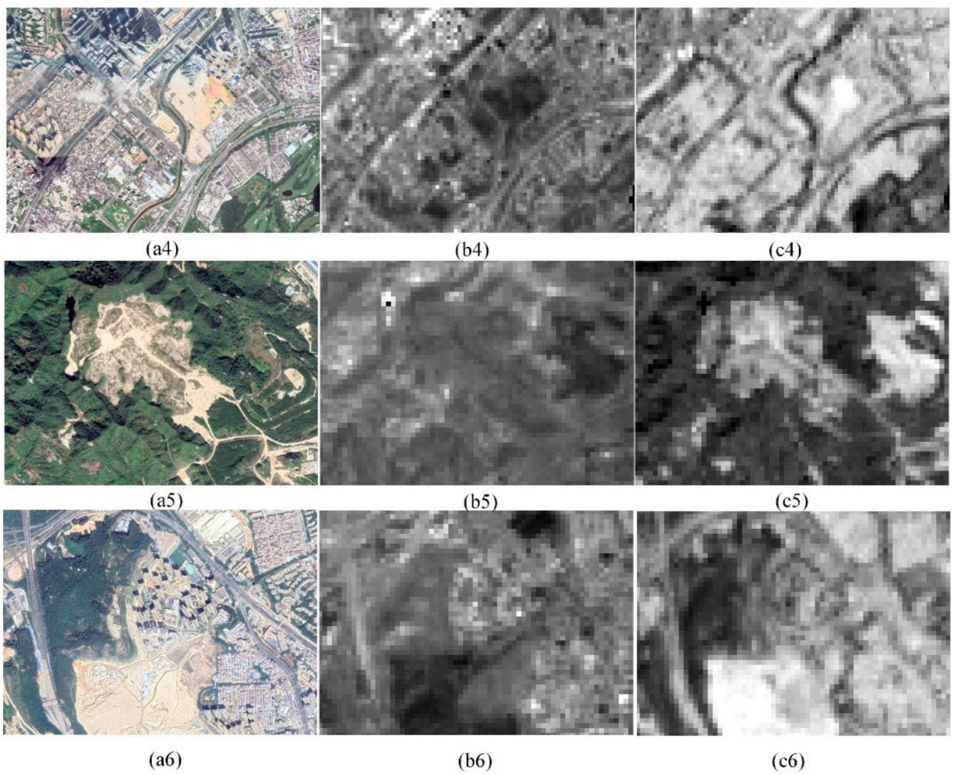

FIGURE 9. Mapping of: (a4 ∼ a6): Google Earth image, (b4 ∼ b6): the value of RNDSI, (c4 ∼ c6) the value of DBSI in (a4 ∼ c4): sample region 4, (a5 ∼ c5): sample region 5, (a6 ∼ c6): sample region 6 in Shenzhen.

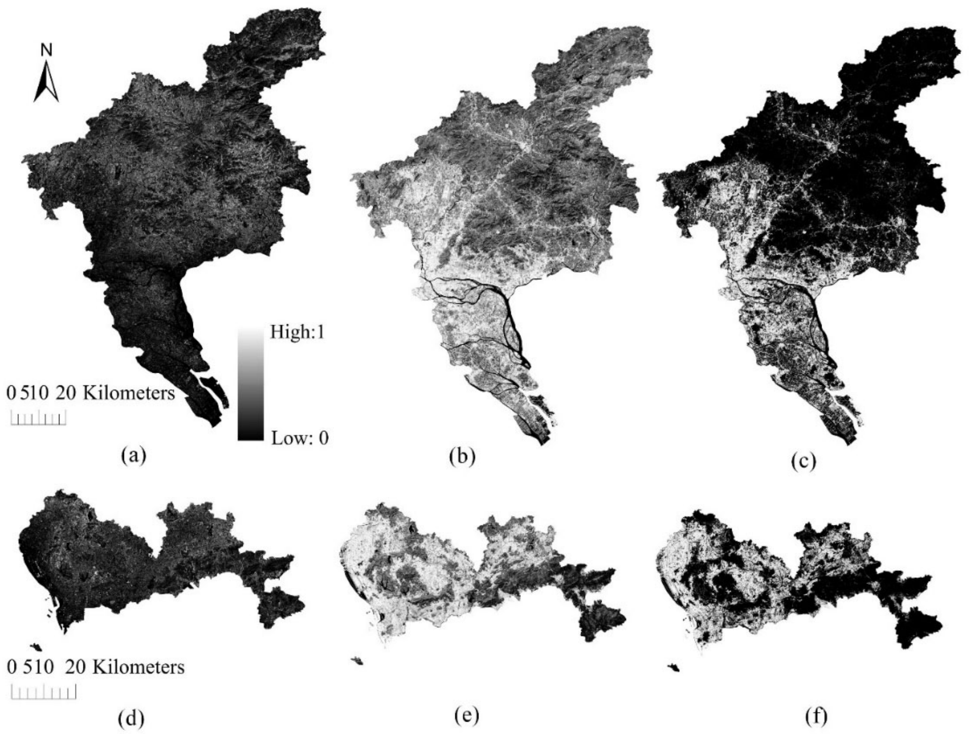

FIGURE 10. Distribution of impervious surface fraction during the modified processing: (a) and (d) impervious surface fraction separated from the soil fraction of LSMA (IS I in Figure 2), (b) and (e) the sum of the impervious surface fraction (the sum of high- albedo fraction and low albedo fraction) of LSMA and impervious surface fraction separated from the soil component of LSMA (IS II in Figure 2), (c) and (f) the final impervious surface fraction by removing soil and vegetation fraction from (b) and (e).

performances of RNDSI and DBSI in the study area, six sampling regions (three in Guangzhou and three in Shenzhen) were selected for detailed assessment, and are shown in Figure 8 and Figure 9.

From Figure 8, in the areas of Guangzhou with soil and vegetation, the DBSI values of soils are higher than those of vegetation, as shown in the sampled region 1, while the RNDSI values of soils are lower than those of vegetation. Minor soil areas are indistinguishable from the vegetation areas in the RNDSI image. In the sampled regions 2 and 3, the DBSI values of soil and IS are higher than those of vegetation, and it is easier to separate vegetation from the result of LSMA. Furthermore, the DBSI values of soil are higher than those of IS and the differences in DBSI values between soil and IS are clearly visible in the details.

The sampled regions 4–6 in Shenzhen exhibit DBSI and RNDSI characteristics similar to those of regions 1–3. From these results, DBSI distinguished land cover types in the study areas better than the RNDSI.

In Guangzhou, the southern central and western central regions represent areas of high urbanization, including the Yuexiu, Liwan, Baiyun, Tianhe, Haizhu, and Huangpu districts. These areas rich in thriving business districts (such as the Guangzhou Tianhe Central Business District) and are characterized by IS coverage of pixels close to 100%. Areas with low urbanization are predominantly in the north and

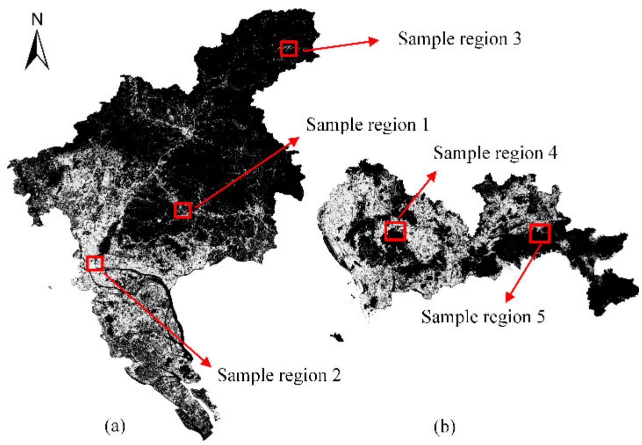

FIGURE 11. Location of the sample regions in: (a) Guangzhou, (b) Shenzhen.

east, including the Zengcheng and Conghua districts, and in forest and farmland areas, where IS coverage of pixels close to 0%. The distribution of IS extracted using LSMA with the post-processing model is consistent with the actual situation in Guangzhou. In pervious areas (forests and farmlands), the IS fractions extracted by LSMA with the post-processing model were near 0%, while in the developed regions (southern central and western central Guanghzou), they were nearly 100%. In Shenzhen, most regions are

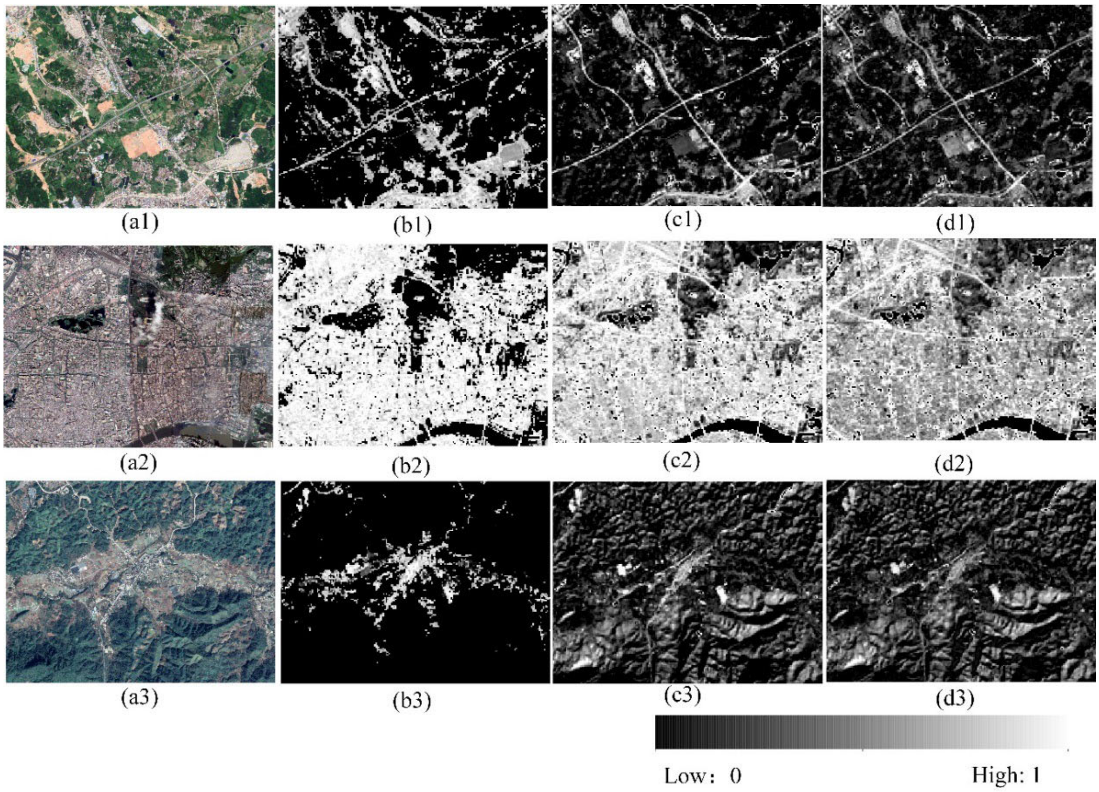

FIGURE 12. Mapping of the impervious surface in (a1 ∼ d1): sample region 1, (a2 ∼ d2): sample region 2, and (a3 ∼ d3): sample region 3 over Guangzhou extracted by: (a1 ∼ a3) Google Earth image, (b1 ∼ b3): the LSMA with Post-processing model, (c1 ∼ c3): the Li's LSMA and (d1 ∼ d3): the conventional LSMA.

experiencing rapid urbanization, and most urban areas yielded high IS coverage. However, in the eastern region, especially the Dapeng Peninsula and Tiantou mountain natural reserves belonging to a forest ecosystem types of natural reserves, forest coverage is higher, and land use as forest is prioritized. The areal ratio is greater than 90% [50], with alternative land use scattered across small areas of arable land, mainly involving eco-tourism development. As a result, IS coverage is low.

By comparing the distributions of DBSI and RNDSI (Figure 10), the former exhibits a higher potential for identifying soil from other land cover types than the latter for Landsat 8 OLI images. Figures 10(a) and (d) show the distributions of the IS fractions (IS I in Figure 2) separated from the soil fraction of the unmixing result using the DBSI threshold value. Owing to spectral information errors associated with pure endmembers, the IS is sometimes mistaken for soil in the LSMA soil fraction. Therefore, the aim of this step was to resolve IS underestimation in urban areas. The distributions of the IS fractions (the sum of the IS fraction from the unmixing result and the IS fraction separated from the soil fraction) corresponding to IS II in Figure 2 are displayed in Figures 10(b) and (e). The IS fraction of the unmixing result is the sum of the high- and low-albedo fractions, and the final IS fractions (IS in Figure 2) are displayed in Figures 10(c) and (f). However, minor amounts of vegetation and soil still exist in Figure 10(b) and (e) owing to unmixing errors. After NDVI and DBSI threshold separation, the soil and vegetation pixels were reincorporated into the soil and vegetation fractions, respectively. Concurrently, to ensure IS fractions in Figures 10(b) and (e) are not altered, pixels for separation are pure, and so the NDVI and DBSI threshold values are set higher than the corresponding theoretical values. In theory, pixels with NDVI values greater than 0 are considered as vegetation, although Azad *et al.* [37] used a DBSI value of 0.1 as the threshold for distinguishing buildings from bare soil. For the study area, NDVI and DBSI values were set to 0.4 and 0.2, respectively, for identifying vegetation and soil based on tests data.

To compare the results of LSMA with the post-processing model with the other methods, five sampling regions in Guangzhou and Shenzhen were selected for further analysis (Figure 11).

Figure 12 and Figure 13 show details of the sampled regions for IS (from Google Earth images and extracted by LSMA with the post-processing model, and by Li's and conventional LSMA from the Landsat 8 OLI respectively). According to the Google Earth images, LSMA with the post-processing model distinguished IS from bare soil and vegetation better than the other approaches, and the post-processing model eliminated IS fraction overestimation of pervious surfaces and effectively minimized its

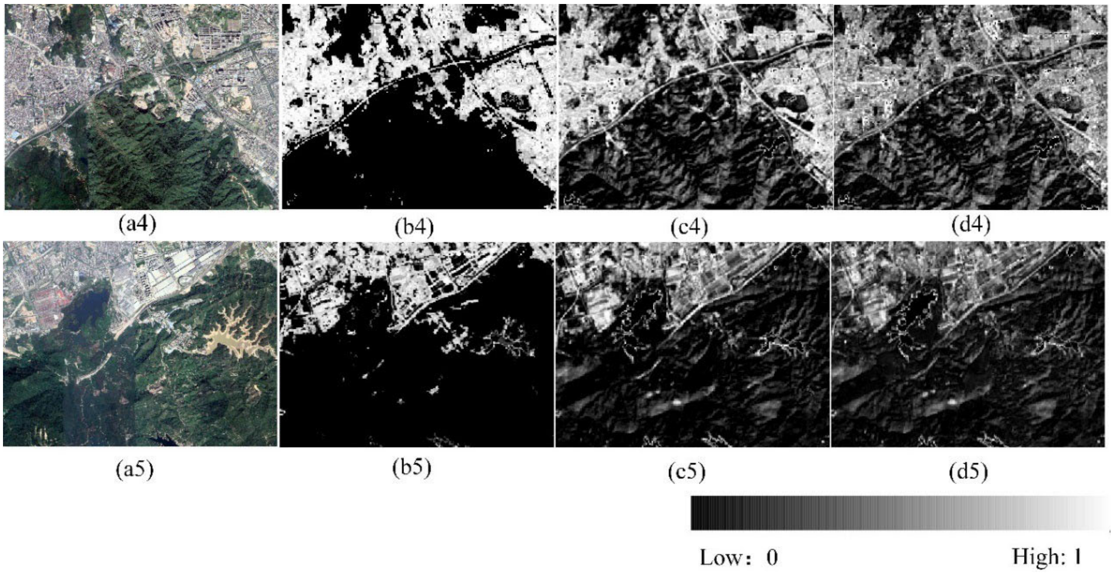

FIGURE 13. **Mapping of the impervious surface in (a1 ∼ d1): sample region 4 and (a2, d2): sample region 5 over Shenzhen extracted by: (a1, a2): Google Earth image, (b1, b2): the LSMA with Post-processing model, (c1, c2): the Li's LSMA and (d1, d2): the conventional LSMA.**

underestimation in urban areas. Simultaneously, LSMA with the post-processing model ensured the integrity of the IS land cover types (e.g., roads and buildings).

In the sampled region 1, since the IS is cross-distributed with vegetation and soil, LSMA with the post-processing model better estimated IS fractions such as roads and buildings, while also removing pervious surface fractions such as farmland and bare soil, thereby preventing IS fraction overestimation in pervious areas. In some urban areas with high building density in the sampled region 2, the IS fractions extracted by the conventional and Li's LSMAs were lower than the actual IS ratios, whereas LSMA with the post-processing model produced ratios mostly near 1. In region 3, because of the spectral features of low-albedo IS and vegetation in some bands, IS fractions in the conventional and Li's LSMAs for large vegetation areas remained clear, while LSMA with the post-processing model eliminated the IS fraction in such areas. The IS distributions for the sampled regions 4 and 5 (Figure 13) confirmed the applicability of LSMA with the post-processing model to Shenzhen.

VI. CONCLUSION

In this study, we developed a post-processing model for improving the extraction of IS fractions using LSMA in Guangzhou and Shenzhen. This approach was developed based on the conventional LSMA and the endmember selection approach proposed by Li *et al.* [36]. The proposed method was tested using data from Landsat 8 OLI images taken on 20 September 2019 (Path/Row: 121/44) and 14 November 2019 (Path/Row: 122/44). By comparing the results from the different methods, the accuracy of the IS fraction extracted by LSMA with the post-processing model was superior, with the method effectively resolving the land cover type misclassification problem. The approach had a very good performance when extracting urban IS fractions, with the highest R2 and lowest RMSE, SE, and MAE values among the tested methods. Furthermore, the method showed superior extraction of IS from vegetation and soil; that is, IS, vegetation, and soil were clearly distinguished, with accurate road extraction in forest areas. The results showed increased IS fractions in impervious areas and decreased fractions in pervious areas, producing IS fraction distributions close to the actual situation. In contrast, the conventional LSMA and Li's LSMA overestimated the IS fraction in pervious areas and underestimated it in impervious areas because of endmember selection errors. DBSI and NDVI threshold selections for the modified processing technique were based on multiple pixel comparison, rather than on a fixed and theoretical approach. In the future, more theoretical data for spectral indices and threshold selection methods will be integrated into LSMA with the post-processing model for land cover type identification and urban IS research enhancement.

REFERENCES

[1] E. Brabec, S. Schulte, and P. L. Richards, "Impervious surfaces and water quality: A review of current literature and its implications for watershed planning," *J. Planning Literature*, vol. 16, no. 4, pp. 499–514, May 2002, doi: 10.1177/088541202400903563.

[2] K. C. Seto, M. Fragkias, B. Güneralp, and M. K. Reilly, "A meta-analysis of global urban land expansion," *PLoS ONE*, vol. 6, no. 8, Aug. 2011, Art. no. e23777, doi: 10.1371/journal.pone.0023777.

[3] J. Xu, Y. Zhao, K. Zhong, H. Ruan, and X. Liu, "Coupling modified linear spectral mixture analysis and soil conservation service curve number (SCS-CN) models to simulate surface runoff: Application to the main urban area of Guangzhou, China," *Water*, vol. 8, no. 12, p. 550, Nov. 2016, doi: 10.3390/w8120550.

[4] C. L. Arnold and C. J. Gibbons, "Impervious surface coverage: The emergence of a key environmental indicator," *J. Amer. Planning Assoc.*, vol. 62, no. 2, pp. 243–258, Jun. 1996, doi: 10.1080/01944369608975688.

[5] A. Buyantuyev, J. Wu, and C. Gries, "Multiscale analysis of the urbanization pattern of the phoenix metropolitan landscape of USA: Time, space and thematic resolution," *Landscape Urban Planning*, vol. 94, nos. 3–4, pp. 206–217, Mar. 2010, doi: 10.1016/j.landurbplan.2009.10.005.

[6] H. Zhang, H. Lin, Y. Zhang, and Q. Weng, *Remote Sensing of Impervious Surfaces: In Tropical and Subtropical Areas*. Terre Haute, IN, USA: CRC Press, 2015.

[7] Q. Weng and D. Lu, "A sub-pixel analysis of urbanization effect on Land Surface Temperature and its interplay with impervious surface and vegetation coverage in indianapolis, united states," *Int. J. Appl. Earth Observ. Geoinf.*, vol. 10, no. 1, pp. 68–83, Feb. 2008, doi: 10.1016/j.jag.2007.05.002.

[8] Z. Dai, J.-M. Guldmann, and Y. Hu, "Spatial regression models of park and land-use impacts on the urban heat island in central Beijing," *Sci. Total Environ.*, vol. 626, pp. 1136–1147, Jun. 2018, doi: 10.1016/j.scitotenv.2018.01.165.

[9] C. Zhao, J. Jensen, Q. Weng, and R. Weaver, "A geographically weighted regression analysis of the underlying factors related to the surface urban heat island phenomenon," *Remote Sens.*, vol. 10, no. 9, p. 1428, Sep. 2018, doi: 10.3390/rs10091428.

[10] L. Yao, W. Wei, Y. U. Yang, J. Xiao, and L. Chen, "Research on potential runoff risk of urban functional zones in Beijing city based on GIS and RS," *Acta Geographica Sinica*, vol. 70, no. 2, pp. 308–318, 2015, doi: 10.11821/dlxb201502011.

[11] G. Y. Gao, B. J. Fu, Y. H. Lü, Y. Liu, S. Wang, and J. Zhou, "Coupling the modified SCS-CN and RUSLE models to simulate hydrological effects of restoring vegetation in the loess plateau of China," *Hydrol. Earth Syst. Sci. Discuss.*, vol. 9, no. 3, pp. 4193–4233, Mar. 2012, doi: 10.5194/hessd-9-4193-2012.

[12] A. Guo, J. Yang, X. Xiao, J. Xia, C. Jin, and X. Li, "Influences of urban spatial form on urban heat island effects at the community level in China," *Sustain. Cities Soc.*, vol. 53, Feb. 2020, Art. no. 101972, doi: 10.1016/j.scs.2019.101972.

[13] Y. Ban and P. Gamba, "EO4Urban: First-year results on Sentinel-1A SAR and Sentinel-2A MSI data for global urban services," in *Proc. Living Planet Symp.*, vol. 2016, p. 114.

[14] L. Zhang, *Estimation of Impervious Surface at Regional Scale Using Landsat Time Series Imagery*. Wuhan, China: Wuhan Univ., 2017.

[15] B. Güneralp, M. Reba, B. U. Hales, E. A. Wentz, and K. C. Seto, "Trends in urban land expansion, density, and land transitions from 1970 to 2010: A global synthesis," *Environ. Res. Lett.*, vol. 15, no. 4, Mar. 2020, Art. no. 044015, doi: 10.1088/1748-9326/ab6669.

[16] F. Fan, Y. Deng, X. Hu, and Q. Weng, "Estimating composite curve number using an improved SCS-CN method with remotely sensed variables in Guangzhou, China," *Remote Sens.*, vol. 5, no. 5, pp. 1425–1437, 2013, doi: 10.3390/rs5031425.

[17] M. K. Ridd, "Exploring a V-I-S (vegetation-impervious surface-soil) model for urban ecosystem analysis through remote sensing: Comparative anatomy for cities," *Int. J. Remote Sens.*, vol. 16, no. 12, pp. 2165–2185, Aug. 1995, doi: 10.1080/01431169508954549.

[18] Q. Weng, "Remote sensing of impervious surfaces in the urban areas: Requirements, methods, and trends," *Remote Sens. Environ.*, vol. 117, pp. 34–49, Feb. 2012, doi: 10.1016/j.rse.2011.02.030.

[19] F. Fan and Y. Deng, "Enhancing endmember selection in multiple endmember spectral mixture analysis (MESMA) for urban impervious surface area mapping using spectral angle and spectral distance parameters," *Int. J. Appl. Earth Observ. Geoinf.*, vol. 36, pp. 103–105, Dec. 2015, doi: 10.1016/j.jag.2014.06.011.

[20] F. Fan, W. Fan, and Q. Weng, "Improving urban impervious surface mapping by linear spectral mixture analysis and using spectral indices," *Can. J. Remote Sens.*, vol. 41, no. 6, pp. 577–586, Nov. 2015, doi: 10.1080/07038992.2015.1112730.

[21] C. Wu, "Normalized spectral mixture analysis for monitoring urban composition using ETM+ imagery," *Remote Sens. Environ.*, vol. 93, no. 4, pp. 480–492, Dec. 2004, doi: 10.1016/j.rse.2004.08.003.

[22] C. Wu and A. T. Murray, "Estimating impervious surface distribution by spectral mixture analysis," *Remote Sens. Environ.*, vol. 84, no. 4, pp. 493–505, 2003, doi: 10.1016/s0034-4257(02)00136-0.

[23] Z. Honglei, L. Ying, and F. Bolin, "Estimating impervious surfaces by linear spectral mixture analysis under semi-constrained condition," in *Proc. Int. Conf. Remote Sensing, Environ. Transp. Eng.*, 2013, pp. 355–358.

[24] Y. Zhao, J. Xu, K. Zhong, Y. Wang, and Q. Zheng, "Extraction of urban impervious surface in Guangzhou by LSMA with NDBI," *Geospatial Inf.*, vol. 16, pp. 90–93, Mar. 2018, doi: 10.3969/j.issn.1672-4623.2018.03.027.

[25] B. Somers, G. P. Asner, L. Tits, and P. Coppin, "Endmember variability in spectral mixture analysis: A review," *Remote Sens. Environ.*, vol. 115, no. 7, pp. 1603–1616, Jul. 2011, doi: 10.1016/j.rse.2011.03.003.

[26] B. Somers, M. Zortea, A. Plaza, and G. P. Asner, "Automated extraction of image-based endmember bundles for improved spectral unmixing," *IEEE J. Sel. Topics Appl. Earth Observ. Remote Sens.*, vol. 5, no. 2, pp. 396–402, Apr. 2012, doi: 10.1109/jstars.2011.2181340.

[27] X. Wu, B. Huang, A. Plaza, Y. Li, and C. Wu, "Real-time implementation of the pixel purity index algorithm for endmember identification on GPUs," *IEEE Geosci. Remote Sens. Lett.*, vol. 11, no. 5, pp. 955–959, May 2014, doi: 10.1109/LGRS.2013.2283214.

[28] C.-l. Chang, C.-C. Wu, and C.-T. Tsai, "Random N-finder (N-FINDR) endmember extraction algorithms for hyperspectral imagery," *IEEE Trans. Image Process.*, vol. 20, no. 3, pp. 641–656, Mar. 2011.

[29] A. Zare and K. C. Ho, "Endmember variability in hyperspectral analysis: Addressing spectral variability during spectral unmixing," *IEEE Signal Process. Mag.*, vol. 31, no. 1, pp. 95–104, Jan. 2014, doi: 10.1109/msp.2013.2279177.

[30] M. K. Sang, H. Y. Sang, S. Ju, and J. Heo, "Monitoring and analyzing water area variation of lake enriquillo, dominican republic by integrating multiple endmember spectral mixture analysis and MODIS data," *Ecol. Resilient Infrastruct.*, vol. 5, no. 2, pp. 59–71, 2018.

[31] Y. Zhou, A. Rangarajan, and P. D. Gader, "A Gaussian mixture model representation of endmember variability in hyperspectral unmixing," *IEEE Trans. Image Process.*, vol. 27, no. 5, pp. 2242–2256, May 2018, doi: 10.1109/TIP.2018.2795744.

[32] P. E. Dennison and D. A. Roberts, "Endmember selection for multiple endmember spectral mixture analysis using endmember average RMSE," *Remote Sens. Environ.*, vol. 87, nos. 2–3, pp. 123–135, 2003, doi: 10.1016/s0034-4257(03)00135-4.

[33] J. Rouse, R. Haas, J. Schell, and D. Deering, *Monitoring Vegetation Systems in the Great Plains with ERTS*, vol. 1. Washington, DC, USA: NASA, 1974.

[34] Y. Zha, J. Gao, and S. Ni, "Use of normalized difference built-up index in automatically mapping urban areas from TM imagery," *Int. J. Remote Sens.*, vol. 24, no. 3, pp. 583–594, Jan. 2003, doi: 10.1080/01431160304987.

[35] Y. Deng, C. Wu, M. Li, and R. Chen, "RNDSI: A ratio normalized difference soil index for remote sensing of urban/suburban environments," *Int. J. Appl. Earth Observ. Geoinf.*, vol. 39, pp. 40–48, Jul. 2015, doi: 10.1016/j.jag.2015.02.010.

[36] H. Li, L. Li, L. Chen, X. Zhou, Y. Cui, Y. Liu, and W. Liu, "Mapping and characterizing spatiotemporal dynamics of impervious surfaces using landsat images: A case study of Xuzhou, east China from 1995 to 2018," *Sustainability*, vol. 11, no. 5, p. 1224, Feb. 2019, doi: 10.3390/su11051224.

[37] H. B. A. Rasul, R. G. F. Ibrahim, M. H. Hameed, J. Wheeler, B. Adamu, S. Ibrahim, and M. P. Najmaddin, "Applying built-up and bare-soil indices from Landsat 8 to cities in dry climates," *Land*, vol. 7, no. 81, pp. 1–13, 2018, doi: 10.3390/land7030081.

[38] *Population Size and Distribution of Guangzhou in 2019*. Accessed: Mar. 11, 2020. [Online]. Available: http://tjj.gz.gov.cn/tjgb/qtgb/content/post_5729556.html

[39] J. Chen. *Shenzhen Became the First City in China to Have no Rural Areas or Farmers*. Accessed: Apr. 21, 2019. [Online]. Available: https://baike.baidu.com/reference/140588/a9f73_lGq3msoesxYAOXVIcQWo93y4DW0SbiWAtZybg_Ly8-DC4xRmw911BDqNosVBKXyIjvXLAdCL_hNxn44R17nqrwNgVt7Qh31fo4HWe01415

[40] E. Vermote, C. Justice, M. Claverie, and B. Franch, "Preliminary analysis of the performance of the landsat 8/OLI land surface reflectance product," *Remote Sens. Environ.*, vol. 185, pp. 46–56, Nov. 2016, doi: 10.1016/j.rse.2016.04.008.

[41] Y. Chen and S. Yu, "Assessment of urban growth in guangzhou using multi-temporal, multi-sensor landsat data to quantify and map impervious surfaces," *Int. J. Remote Sens.*, vol. 37, no. 24, pp. 5936–5952, Dec. 2016, doi: 10.1080/01431161.2016.1252473.

[42] H.-Q. Xu, "A study on information extraction of water body with the modified normalized difference water index (MNDWI)," *J. Remote Sens.*, vol. 9, pp. 589–595, Sep. 2005.

[43] N. Otsu, "A threshold selection method from gray-level histograms," *IEEE Trans. Syst., Man, Cybern.*, vol. SMC-9, no. 1, pp. 62–66, Jan. 1979, doi: 10.1109/TSMC.1979.4310076.
[44] C.-I. Chang and A. Plaza, "A fast iterative algorithm for implementation of pixel purity index," *IEEE Geosci. Remote Sens. Lett.*, vol. 3, no. 1, pp. 63–67, Jan. 2006, doi: 10.1109/LGRS.2005.856701.
[45] C. Yang, J. Wang, L. Qu, X. Sun, and S. LI, "Research on the extraction of surface feature abundance based on the least square mixed pixel decomposition," *Sci. Surveying Mapping*, vol. 42, no. 9, pp. 143–150, 2017, doi: 10.16251/j.cnki.1009-2307.2017.09.026.
[46] F. Fan, "The application and evaluation of two methods based on LSMM model—A case study in Guangzhou," *Remote Sens. Technol. Appl.*, vol. 23, no. 3, pp. 272–277, 2008, doi: 10.3724/SP.J.1087.2008.01721.
[47] M. H. A. Baig, L. Zhang, T. Shuai, and Q. Tong, "Derivation of a tasselled cap transformation based on Landsat 8 at-satellite reflectance," *Remote Sens. Lett.*, vol. 5, no. 5, pp. 423–431, May 2014, doi: 10.1080/2150704x.2014.915434.
[48] C. Deng and C. Wu, "BCI: A biophysical composition index for remote sensing of urban environments," *Remote Sens. Environ.*, vol. 127, pp. 247–259, Dec. 2012, doi: 10.1016/j.rse.2012.09.009.
[49] C. Deng and C. Wu, "Examining the impacts of urban biophysical compositions on surface urban heat island: A spectral unmixing and thermal mixing approach," *Remote Sens. Environ.*, vol. 131, pp. 262–274, Apr. 2013, doi: 10.1016/j.rse.2012.12.020.
[50] Z. Wang, Y. Huang, L. Yang, C. Sun, H. Sun, X. Liu, W. Zhang, and X. Gan, "Dynamics of land use and landscape pattern of forest ecosystem nature reverse in Shenzhen in Rencent 20 years," *Forestry Environ. Sci.*, vol. 35, no. 2, pp, pp. 1–6, 2019.

YI ZHAO was born in China, in 1992. She is currently pursuing the Ph.D. degree with the Guangzhou Institute of Geochemistry, Chinese Academy of Sciences, Guangzhou, China. She has published several conference and journal articles. Her research interests include hyperspectral remote sensing and urban impervious surfaces.

JIANHUI XU received the Ph.D. degree from Wuhan University, Wuhan, China. He is currently an Associate Professor with the Guangzhou Institute of Geography. He has published numerous SCI articles in prestigious journals, such as *Remote Sensing* in impervious surfaces. His research interests include road surface models, impermeable water surfaces, and urban remote sensing. He received the Pearl River Talent Award in Guangdong Province.

KAIWEN ZHONG graduated in photogrammetry and remote sensing from Wuhan University, Wuhan, China. He is currently a Professor with the Guangzhou Institute of Geography, the Director with the Chinese Society of Geographic Information Systems, the Executive Director with the Guangdong Society of Remote Sensing and Geographic Information Systems, the Director with the Guangdong Society of Geography, and the Leader with the Public Laboratory of Guangdong Geospatial Information and the Guangdong Key Laboratory of Remote Sensing and Geographic Information Systems. He has presided over the completion of more than 20 projects, including the National Natural Science Foundation of China, the Guangdong Natural Science Foundation, the Guangdong Province Science and Technology Project, and the Guangdong Province and Chinese Academy of Sciences Guangdong Province Science and Technology Project. He has published more than 40 articles in multiple countries. He has one coauthored monograph and applied for and authorized four software copyrights. His research interests include impermeable water surfaces, urban remote sensing, and agricultural remote sensing. He received two provincial and higher scientific and technological progress awards.

YUNPENG WANG was born in Shanxi, China, in 1968. He received the B.S. degree in geology from Lanzhou University, Lanzhou, China, in 1990, and the M.S. and Ph.D. degrees in remote sensing and geochemistry from the Guangzhou Institute of Geochemistry, Chinese Academy of Sciences (GIGCAS), Guangzhou, China, in 1992 and 1996, respectively.

He was a Visiting Scholar with the Imperial College London, London, U.K., and the Brookhaven National Laboratory, Upton, NY, USA, in 2003 and 2004, respectively. He has been with GISCAS, since 1996, where he has been a Research Professor, since 2002. He is also currently an Affiliate Professor with the Graduate University of CAS, Beijing, China. His main research interests include remote sensing and applications on environment, geology, and geochemistry. He has published more than 100 articles in international journals.

Dr. Wang was a recipient of the Second-Rank Award from the National Sciences and Technology Progress of China.

HONGDA HU received the Ph.D. degree from Wuhan University, Wuhan, China. He is currently an Assistant Researcher with the Guangzhou Institute of Geography. He has also published science citation index (SCI) articles in prestigious journals, such as *Science of the Total Environment* in satellite remote sensed PM2.5 modeling. His research interests include spatiotemporal statistics and environmental remote sensing. He received the national natural science funds.

PINGHAO WU was born in China, in 1995. She is currently pursuing the Ph.D. degree with the Guangzhou Institute of Geochemistry, Chinese Academy of Sciences, Guangzhou, China. Her research interests include remote sensing interpretation, deep learning, remote sensing application, and environmental remote sensing.